

Evaluation of Microphysics Schemes in Tropical Cyclones Using Polarimetric Radar Observations: Convective Precipitation in an Outer Rainband

DAN WU,^{a,b,c,d} FUQING ZHANG,^d XIAOMIN CHEN,^e ALEXANDER RYZHKOV,^f KUN ZHAO,^{b,c}
MATTHEW R. KUMJIAN,^d XINGCHAO CHEN,^d AND PAK-WAI CHAN^g

^a Shanghai Typhoon Institute, Shanghai, China

^b Key Laboratory of Mesoscale Severe Weather/MOE and School of Atmospheric Sciences, Nanjing University, Nanjing, China

^c State Key Laboratory of Severe Weather and Joint Center for Atmospheric Radar Research of CMA/NJU, Beijing, China

^d Department of Meteorology and Atmospheric Science, The Pennsylvania State University, University Park, Pennsylvania

^e Hurricane Research Division, NOAA/AOML, Miami, Florida

^f Cooperative Institute for Mesoscale Meteorological Studies, University of Oklahoma, Norman, Oklahoma

^g Hong Kong Observatory, Kowloon, Hong Kong, China

(Manuscript received 14 November 2019, in final form 13 January 2021)

ABSTRACT: Cloud microphysics significantly impact tropical cyclone precipitation. A prior polarimetric radar observational study by the authors revealed the ice-phase microphysical processes as the dominant microphysics mechanisms responsible for the heavy precipitation in the outer rainband of Typhoon Nida (2016). To assess the model performance regarding microphysics, three double-moment microphysics schemes (i.e., Thompson, Morrison, and WDM6) are evaluated by performing a set of simulations of the same case. While these simulations capture the outer rainband's general structure, microphysics in the outer rainbands are strikingly different from the observations. This discrepancy is primarily attributed to different microphysics parameterizations in these schemes, rather than the differences in large-scale environments due to cloud–environment interactions. An interesting finding in this study is that the surface rain rate or liquid water content is inversely proportional to the simulated mean raindrop sizes. The mass-weighted raindrop diameters are overestimated in the Morrison and Thompson schemes and underestimated in the WDM6 scheme, while the former two schemes produce lower liquid water content than WDM6. Compared with the observed ice water content based on a new polarimetric radar retrieval method, the ice water content above the environmental 0°C level in all simulations is highly underestimated, especially at heights above 12 km MSL where large concentrations of small ice particles are typically prevalent. This finding suggests that the improper treatment of ice-phase processes is potentially an important error source in these microphysics schemes. Another error source identified in the WDM6 scheme is overactive warm-rain processes that produce excessive concentrations of smaller raindrops.

KEYWORDS: Tropical cyclones; Cloud microphysics; Radars/Radar observations; Model evaluation/performance

1. Introduction

Landfalling tropical cyclones (TC) are among the most devastating weather systems around the world. With high precipitation efficiency, the potential for torrential rainfall and freshwater flooding during their landfall tends to cause severe damage to coastal areas. One recent example is Hurricane Florence (2018), which brought a precipitation accumulation of ~913 mm in Elizabethtown, North Carolina, during its landfall. At least 54 people were killed by this storm, and the estimated economic losses in the Carolinas exceeded \$17.9 billion (USD), which is partly attributed to the extreme precipitation. Such a catastrophic impact accentuates the necessity of accurate prediction of landfalling TCs and their associated precipitation. However, while the forecast skill for TC track and intensity have been improved steadily in the past few decades (e.g., Franklin et al. 2003; DeMaria et al. 2005), precipitation forecast skill still lags behind as quantitative

precipitation forecasts remain extremely challenging (e.g., Duan and Liu 2010).

Nowadays, the numerical models with sophisticated physical parameterization schemes are among the most prevalent tools for TC precipitation forecasts. The intensity of surface precipitation in TCs is closely related to microphysical processes occurring in the entire column within the storm, including warm-rain processes below the freezing level and cold-rain processes above. However, most microphysics schemes are based on empirical knowledge derived from observations obtained within non-TC clouds (McFarquhar and Black 2004). Therefore, accurate precipitation forecasts rely heavily upon whether the microphysics schemes can properly represent these microphysical processes in real TCs.

To evaluate simulated TC microphysics in numerical models, two types of observational datasets are available. The first type is in situ observations, such as airborne or surface-based instruments. These observations are more direct than remote sensing platforms such as radars, and the measurements include the size, concentration, and particle types. However, such observations are infrequently collected and limited by their relatively small number of datasets. Moreover, they can only represent the conditions over a small area. The second

Zhang: Deceased.

Corresponding author: Dr. Kun Zhao, zhaokun@nju.edu.cn

DOI: 10.1175/MWR-D-19-0378.1

© 2021 American Meteorological Society. For information regarding reuse of this content and general copyright information, consult the [AMS Copyright Policy](#) (www.ametsoc.org/PUBSReuseLicenses).

type is remote sensing observations, such as ground-based radar reflectivity data. Previous studies have evaluated model simulations by comparing the simulated reflectivity factor (Z_H) with radar observations and found that the simulated Z_H was usually higher than in observations (e.g., McFarquhar et al. 2006, 2012; Chen et al. 2017). Whereas Z_H is a combined manifestation of the size and number concentration of particles within a radar sampling volume, recently upgraded polarimetric radars allow much deeper insight into microphysics by providing additional valuable information about the bulk particle size, shape, and orientation (e.g., Kumjian 2013). One polarimetric radar variable is differential reflectivity (Z_{DR}), defined as the logarithmic ratio of the reflectivity factors at horizontal and vertical polarizations. Z_{DR} is a measure of the reflectivity-weighted mean particle size in the sampling volume, and is insensitive to hydrometeor concentration. For example, rainfall characterized by larger median raindrop diameter will have larger observed Z_{DR} values (Seliga and Brangi 1976; Doviak and Zrnić 1993; Kumjian 2013), as larger raindrops become more oblate than smaller ones owing to deformation by aerodynamic drag. The combination of Z_H and Z_{DR} thus can provide information characterizing the drop size distribution (DSD), as well as “fingerprints” of microphysical processes such as evaporation, coalescence, and breakup (Kumjian and Ryzhkov 2010; Kumjian and Prat 2014). As such, these observations have been used to validate the microphysical characteristics of the simulated TC precipitation. For example, Brown et al. (2016) evaluated 6 different microphysics schemes in the Weather Research Forecast (WRF) Model and found that most of the schemes tend to produce a higher frequency of larger raindrops than observations when viewed in the broad TC scale.

However, previous observational studies suggest that the microphysical characteristics of TC precipitation vary considerably in space and thus so do the microphysical processes accounting for the heavy precipitation (Black and Hallett 1986; May et al. 2008; Houze 2010; Wang et al. 2016; Kalina et al. 2017; Didlake and Kumjian 2017, 2018; Wu et al. 2018; Feng and Bell 2019). By examining polarimetric radar observations of Typhoon Nida (2016), Wu et al. (2018) identified ice-phase microphysical processes as the major pathway of particle growth in the outer rainbands, whereas warm-rain processes dominated in the inner rainband. These differences highlight the necessity of performing a feature-based evaluation to further understand the performance of the microphysics schemes for TC precipitation.

In this study, we will evaluate the simulated microphysics in the outer rainband of Typhoon Nida (2016) based on polarimetric radar observations. Our goal is to answer the following questions: 1) Are the simulated raindrop size distributions in different microphysics schemes consistent with observations? 2) How do the simulated DSDs impact the surface precipitation intensity? 3) Which is the dominant factor responsible for these differences, the differences in microphysics or synoptic environments after a sufficient time of forward integration? 4) Which microphysical processes are responsible for the model-observation discrepancies?

The remainder of the paper is organized as follows. A description of the polarimetric radar datasets and numerical

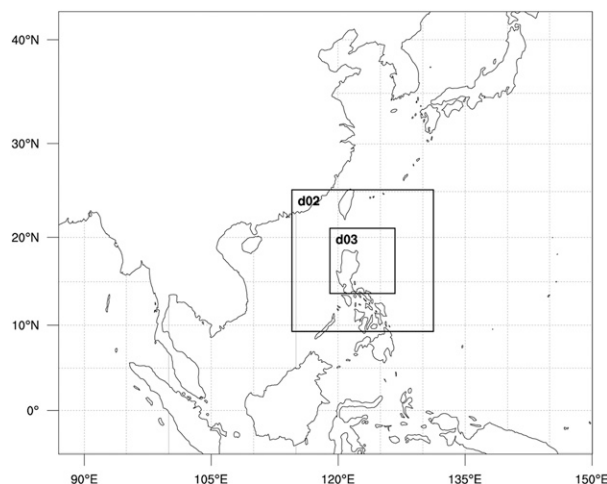


FIG. 1. Triply nested domain settings used for Typhoon Nida (2016) simulations. The innermost two nests automatically move to follow the simulated TC.

simulations is presented in section 2. Comparisons between the polarimetric radar observations and the model simulations, and the potential factors responsible for their differences are discussed in detail in section 3. A summary of the results and implications for TC forecasts are discussed in the conclusions.

2. Data and methods

a. Model setup and experiment design

Typhoon Nida is simulated using the WRF-ARW Model (Skamarock et al. 2008), version 3.9. Two-way interactive triply nested domains are utilized with horizontal grid spacings of 18, 6, and 2 km, consisting of 367×304 , 292×292 , and 403×403 grid points, respectively (Fig. 1). The outermost domain is fixed, while the inner two domains move with the simulated TC. All three domains contain 51 sigma levels, with the highest level at 50 hPa. To match the radar dataset, the model output is interpolated to a constant altitude grid with a 0.5 km vertical spacing. The outer two domains run from 0000 UTC 31 July to 0000 UTC 2 August, whereas the innermost domain is activated 12 h later and runs from 1200 UTC 31 July to 0000 UTC 2 August. The simulations are initialized with the Global Forecast System (GFS) FNL datasets for the initial and lateral boundary conditions. The physics configurations for this study are as follows: the Kain–Fritsch cumulus parameterization scheme (Kain and Fritsch 1993) in the outermost domain; and the Yonsei University (YSU) planetary boundary layer scheme (Hong et al. 2006), the Dudhia shortwave radiation (Dudhia 1989), and the Rapid Radiative Transfer Model (RRTM) longwave radiation scheme (Mlawer et al. 1997) in all three domains.

To evaluate the performance of numerical representations of TC rainband microphysics, we employ 3 bulk microphysics parameterization schemes: the WRF 6-class double-moment scheme (WDM6) (Lim and Hong 2010), the Morrison double-moment scheme (Morrison et al. 2009), and the Thompson

TABLE 1. Design of experiments with different microphysics schemes.

Expt	Description
Thompson	Initialized with Thompson scheme at 0000 UTC 31 Jul 2016
Morrison	As in Thompson, but with Morrison scheme
WDM6	As in Thompson, but with WDM6 scheme
Thom+Morr	Initialized with Thompson scheme, but replaced with Morrison scheme at 0600 UTC 1 Aug 2016
Thom+WDM6	As in Thom+Morr, but replaced with WDM6 scheme

double-moment scheme (Thompson et al. 2008). All the three microphysics schemes predict the same set of mass variables, including cloud water, ice, rain, snow, and graupel. They also predict a second moment (i.e., number concentration) for rainwater. In the Thompson scheme, the size distribution of snow is a combination of two gamma functions and the density of snow varies inversely with diameter. The other species follow an inverse-exponential size distribution. In the Morrison scheme, the cloud droplet size distribution follows a gamma function while the other species are set as inverse-exponential distribution. In the WDM6 scheme, the size distribution for raindrops follows a gamma function with the shape parameter $\mu = 1$. Since different microphysical processes in each microphysical scheme can lead to an increasing discrepancy in the synoptic environment after more than one day's model integration due to cloud-radiative feedbacks and the response to the microphysical diabatic heating, two extra experiments are designed to test the impact of the different synoptic environments on microphysical characteristics of the precipitation. These two experiments are initialized with Thompson scheme and then replaced by Morrison or WDM6 at 0600 UTC 1 August, 3 h before the analysis time. Details of the five experiments are listed in Table 1.

b. Radar data and data processing

Observations of Nida (2016) were collected by two S-band radars located at Guangzhou (hereafter GZRD) and Shenzhen (hereafter SZRD), China, during the field campaign of World Meteorological Organization's (WMO) research and development project: Understanding and Prediction of Rainfall Associated with landfalling Tropical cyclones (UPDRAFT). GZRD is a radar newly upgraded with polarimetric capabilities. The locations of these two radars are denoted as black triangles in Fig. 3a. Both radars complete the volume scan of nine elevations (0.5°, 1.5°, 2.4°, 3.3°, 4.3°, 6.0°, 9.9°, 14.6°, and 19.5°) in 6 min. The radial resolutions for reflectivity and radial velocity are 1 and 0.25 km, respectively. The angular resolution was 1°. The method for the calibration of the radar data has been documented in Huang et al. (2017). After rigorous quality control, the radar data are interpolated onto the Cartesian grids with 1.0 km horizontal and 0.5 km vertical spacing using the Radx2Grid component within the LROSE Software Suite (available at <http://lrose.net/index.html>) with the reorder configuration (Oye et al. 1995). The data collected by the

Hong Kong polarimetric radar (HKRD, marked as gray triangle in Fig. 3a) were used to make an intercomparison with the dataset of the GZRD and results show that these two datasets are generally consistent with each other (not shown). Thus, we only use the polarimetric observations from GZRD in the following analysis. The performance of the model simulations is evaluated against the observations averaged over the period from 1000 to 1100 UTC 1 August. The evaluation period for model simulation is selected when the modeled TC center is closest to the observed TC. For the WDM6 simulation, this period is from 1100 to 1200 UTC 1 August, whereas for other experiments it is from 0900 to 1000 UTC. To compare the characteristics of the different precipitation regimes, the observations and simulated precipitation fields are separated into convective and stratiform regions by using the Z_H -based objective separation algorithm proposed by Steiner et al. (1995). This algorithm is based on the spatial uniformity and intensity of Z_H at 3 km height. The reflectivity threshold used in this study is 40 dBZ. However, some grid points with reflectivity above 50 dBZ are labeled as "stratiform" precipitation. This is because the algorithm is based solely on the Z_H at 3 km altitude, while data points under 3 km are occasionally above 40 dBZ due to the variation of reflectivity in the vertical direction. To fix this issue, grid point with the reflectivity larger than 40 dBZ in a column below the freezing level is classified as convection. Dual-Doppler synthesis (Ray et al. 1978) is applied to retrieve the three-dimensional wind fields in the rainband. The horizontal component of the wind field is retrieved from the radial velocities observed by GZRD and SZRD using the Cartesian Editing and Display of Radar Data under Interactive Control (CEDRIC) software (Mohr et al. 1986). The vertical velocities are obtained through the anelastic continuity equation with the vertical velocity at the echo top set to zero. Data with cross-beam angle $< 30^\circ$ are excluded to reduce the uncertainties and errors in the retrieved winds (Doviak and Zrnić 1993).

c. Simulated polarimetric radar variables

The polarimetric radar forward operator developed by Jung et al. (2010) is utilized to convert the WRF output to polarimetric radar variables. The operator is based on T-matrix scattering calculations for spheroids representing hydrometeors, integrating over the simulated size distributions. The output of this forward operator includes the reflectivity factor at horizontal and vertical polarizations (Z_H and Z_V), differential reflectivity (Z_{DR}), specific differential phase (K_{DP}), and copolar cross-correlation coefficient (ρ_{HV}). After this conversion, the model output can be compared directly with polarimetric radar observations (Brown et al. 2016). Since the forward operator has a substantial uncertainty when ice phase hydrometeors are present, only data points under 3 km altitude, where ice particles are rare, are taken in the analysis.

d. Rain and ice water content estimation

To estimate the liquid water content (LWC) from polarimetric radar measurements, the method mentioned in

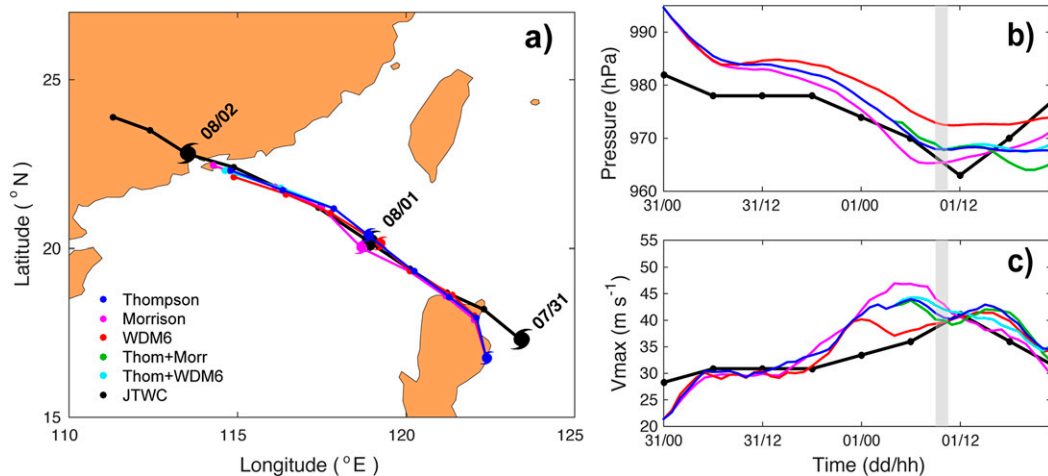


FIG. 2. Verification of simulated (a) tracks, (b) minimum SLP (hPa), and (c) 10 m maximum wind speed (m s^{-1}). The black line represents the best track datasets of JTWC, and the colored lines denote the simulations using different microphysics scheme. The gray box in (b) and (c) denotes the analysis period of 1000–1100 UTC 1 Aug for radar observations.

Zhang (2016) is applied to GZRD observations. The LWC is estimated from the combination of gridded Z_H and Z_{DR} :

$$\text{LWC} = 1.38 \times 10^{-3} Z_H \times 10^{(-2.43Z_{DR} + 1.12Z_{DR}^2 - 0.176Z_{DR}^3)}. \quad (1)$$

This relationship is only applicable for pure raindrops, and is inaccurate in the melting layer or above where raindrops are mixed with ice particles. For LWC varying between 0.1 and 1.0 g m^{-3} , the average fractional standard error of the LWC estimate is about 35% (Ryzhkov et al. 2020).

For the estimation of the ice water content (IWC), a new method proposed by Ryzhkov et al. (2018) is adopted in this study. In this method, the IWC is retrieved from K_{DP} and Z_{dr} (Z_{DR} expressed in linear units):

$$\text{IWC} \approx 4.0 \times 10^{-3} \frac{K_{DP} \lambda}{1 - Z_{dr}^{-1}}, \quad (2)$$

where λ is the radar wavelength expressed in mm. The detailed discussion for the uncertainty of estimates using this method can be found in Ryzhkov et al. (2018). In that study, 11 types of ice crystals with different shapes and orientations are tested and the result shows that this estimation is insensitive to the ice particle's aspect ratios and orientations, but can be affected by the degree of riming. Thus, this method is expected to work better at relatively low temperatures with a lower likelihood of riming. Additionally, this method is applicable for pristine ice crystals or those that exhibit stronger polarimetric contrasts; for heavily aggregated snow (where Z_{DR} and K_{DP} are driven toward zero), the method will underestimate IWC. Moreover, this method is sensitive to possible Z_{DR} errors if Z_{DR} is low (e.g., the Z_{DR} is miscalibrated or not appropriately corrected for noise at the periphery of a radar echo with low signal-to-noise ratio). To prevent blowing up the IWC estimates, a Z_{DR} floor of 0.3 dB is set if $Z_{DR} < 0.3$ dB.

3. Results and discussion

a. Model simulated intensity, tracks, and outer rainband structure of Nida

Figure 2a compares the simulated tracks from the five experiments with the best track from the Joint Typhoon Warning Center (JTWC) Best Track dataset at 6-h intervals. The simulated tracks of all experiments agree well with the best track. The 6-hourly TC track from each simulation almost overlaps with the best track. The track from WDM6 is slightly slower than that from other simulations. Figures 2b and 2c shows the evolution of the minimum sea level pressure and 10 m maximum wind speed from the simulation, as compared with the best track. The simulated TCs intensify more rapidly than observations after 1800 UTC 31 July. However, the general features of intensity evolution of Typhoon Nida (2016) in terms of the minimum sea level pressure and 10 m maximum wind speed are captured. Particularly, the simulated 10 m maximum wind speed is comparable to that from the JTWC best track over the 1 h analysis period (i.e., 1000–1100 UTC 1 August).

Figure 3 compares the simulated TC outer rainband with observations in terms of radar reflectivity. Figure 3a shows the composite of Z_H from two radars at 3 km altitude of Typhoon Nida at 1000 UTC 1 August. In Fig. 3a, a strong rainband is observed at a radial distance of ~ 250 km from the TC center. The three single-scheme experiments (Figs. 3b–d) all reproduce the observed rainband structure over land and the magnitude of radar reflectivity is comparable to the observed value. However, the area coverage of the simulated rainbands is different: the Morrison scheme produces the widest rainband as a mixture of convective and stratiform precipitation and WDM6 has the narrowest rainband, which appears to be more convective in nature.

Figures 3e and 3f show the simulated rainbands from the experiments in which microphysics schemes are changed 3 h prior to the analysis period. Recall that these experiments are initialized with the Thompson scheme in order to obtain the

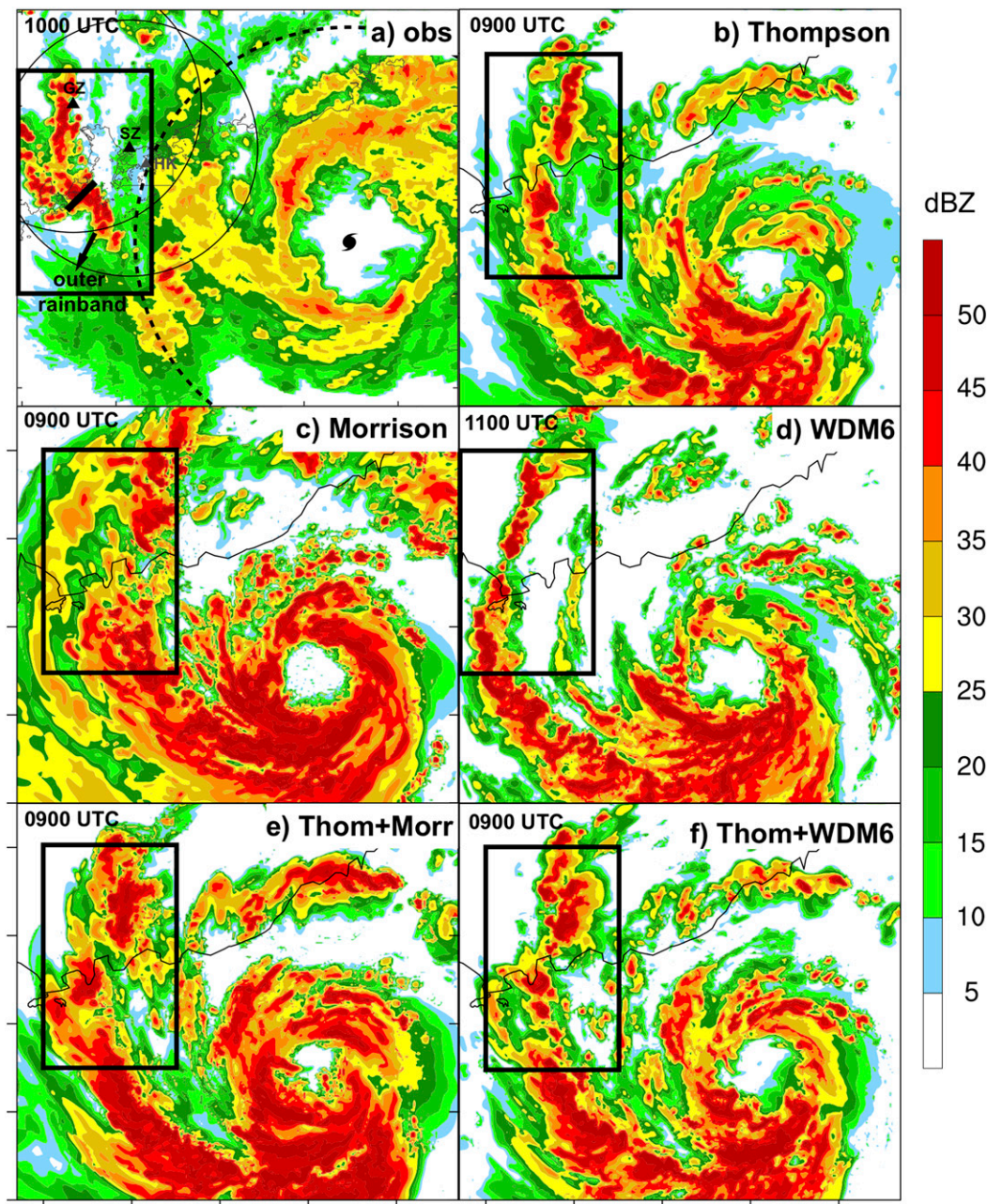


FIG. 3. (a) The 3 km radar reflectivity of Typhoon Nida (2016) at 1000 UTC 1 Aug. The hurricane symbol denotes the TC center at 1000 UTC and the dashed circle marks the 250 km radius from TC center. Locations of the GZRD and SZRD are marked by the black triangles, and the radius of the circle around each radar site is 150 km. Location of HKRD is marked by a gray triangle. The short black line is an example of the vertical slice along the motion vector of the outer rainband. (b)–(f) The simulated reflectivity in each experiment at the time when the TC center is closest to observation in (a). The black box in each panel denotes the analysis domain of the outer rainband.

same large-scale environmental conditions, and 3 h before the analysis time, the Thompson scheme is replaced by the Morrison (Thom+Morr) or WDM6 (Thom+WDM6) scheme. With such a constraint on the large-scale environment, the rainband structures from Thom+Morr and Thom+WDM6 become more similar to Thompson. These experiments thereby provide an

optimal chance to gain insight into the differences in the microphysics between various microphysics schemes.

b. Evaluation of distribution in Z_H – Z_{DR} phase space

Since the outer rainband structure is successfully reproduced in all the experiments, a joint probability density function

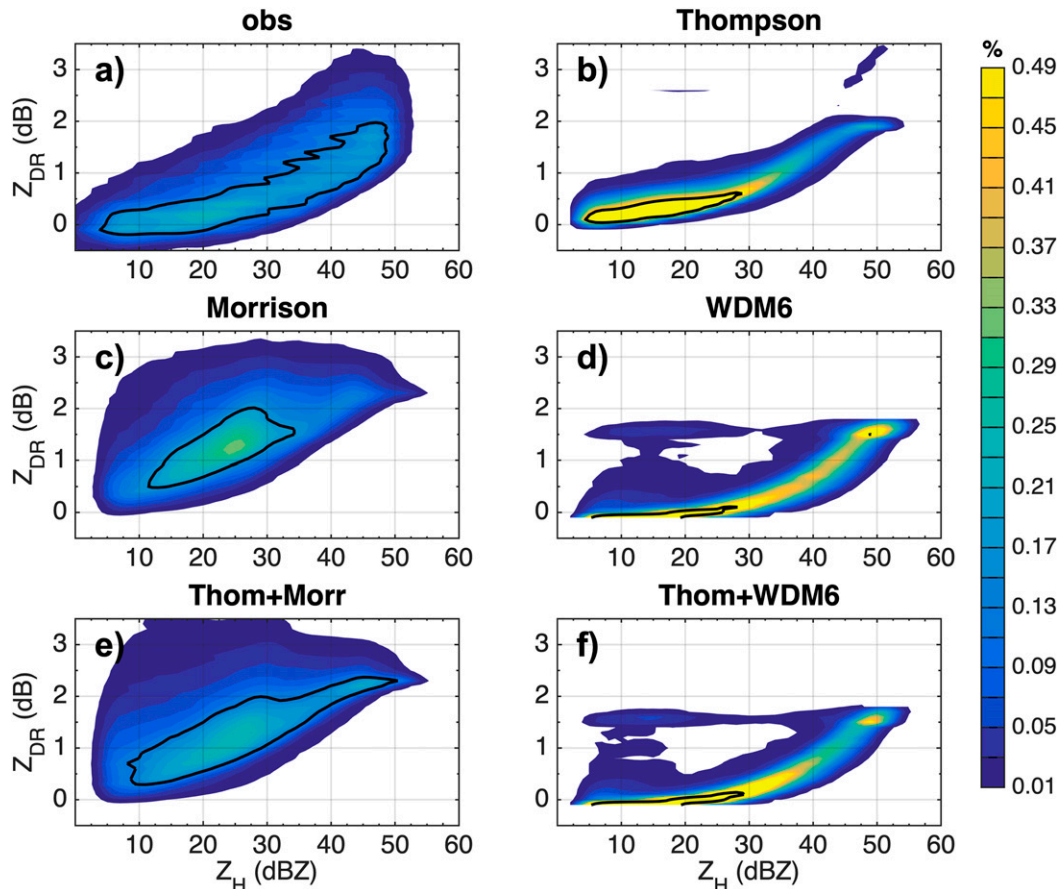


FIG. 4. Joint frequency distributions of Z_H and Z_{DR} for the outer rainband of Typhoon Nida (2016). (a) Radar observations, and simulated observations derived from the WRF Model output using (b) Thompson, (c) Morrison, (d) WDM6, (e) Thom+Morr, and (f) Thom+WDM6 microphysics schemes. Statistics from observation and WRF output are both limited to below 3 km. Z_H is binned from 0 to 60 dBZ every 1 dBZ and Z_{DR} is binned from -0.5 to 3.5 dB every 0.1 dB.

(PDF) is created in Z_H – Z_{DR} space in each dataset to quantitatively evaluate the microphysics from different experiments. As the horizontal resolution of the radar data (1 km) is different from the model output (2 km), the horizontal resolution of the radar data is changed to 2 km by using arithmetic average in this comparison. Each point in this phase-space diagram (Fig. 4) represents a unique DSD through the combination of Z_H – Z_{DR} (Brown et al. 2016), so it can be used to verify the model's ability in representing bulk microphysical properties of the precipitation. The difference from Brown et al. (2016) is that the shading represents the frequency of each point instead of the relative frequency normalized by the maximum frequency in each dataset. Therefore, the value of the frequency in the diagram can be directly compared across each experiment. The black contour in each panel denotes the modal distribution (frequencies greater than 50% of the maximum value within that dataset) following Brown et al. (2016).

In Fig. 4a, the PDF of the observed Z_H and Z_{DR} is characterized by the modal distribution extending from 5 to 50 dBZ in Z_H and from -0.1 to 2 dB in Z_{DR} . From 10 to 20 dBZ in Z_H , the Z_{DR} value for the peak frequency is almost constant around

0.1 dB, whereas from 20 to 50 dBZ, the Z_{DR} value for the peak frequency increased with Z_H . For Thompson (Fig. 4b), the modal distribution ranging from 10 to 25 dBZ almost overlaps with the observations, while the value of frequency is higher than the observations and the range of Z_{DR} is much narrower. The peak frequency for higher Z_H is also concentrated at similar Z_{DR} as the observations, but with a narrower distribution. Also, the frequency of larger Z_{DR} values at greater Z_H is underestimated by the Thompson scheme. For Morrison (Fig. 4c), the PDF distribution is centered around 25 dBZ in Z_H and 1.3 dB in Z_{DR} . The Z_{DR} values for the peak frequency increase with Z_H (from 10 to 50 dBZ) and are much higher than observation. For WDM6 (Fig. 4d), the peak value of frequency is concentrated around 0 dB in Z_{DR} ranging from 10 to 25 dB in Z_H . The Z_{DR} value is truncated under 1.8 dB due to the gamma distribution assumption for raindrops in the WDM6 scheme. The comparison of Figs. 4a–d shows that the microphysical properties of the simulated rainband by the three double-moment microphysics schemes all differ from the observations. A comparison with Brown et al. (2016) shows that, although the simulated Z_{DR} values are still larger than the observed in

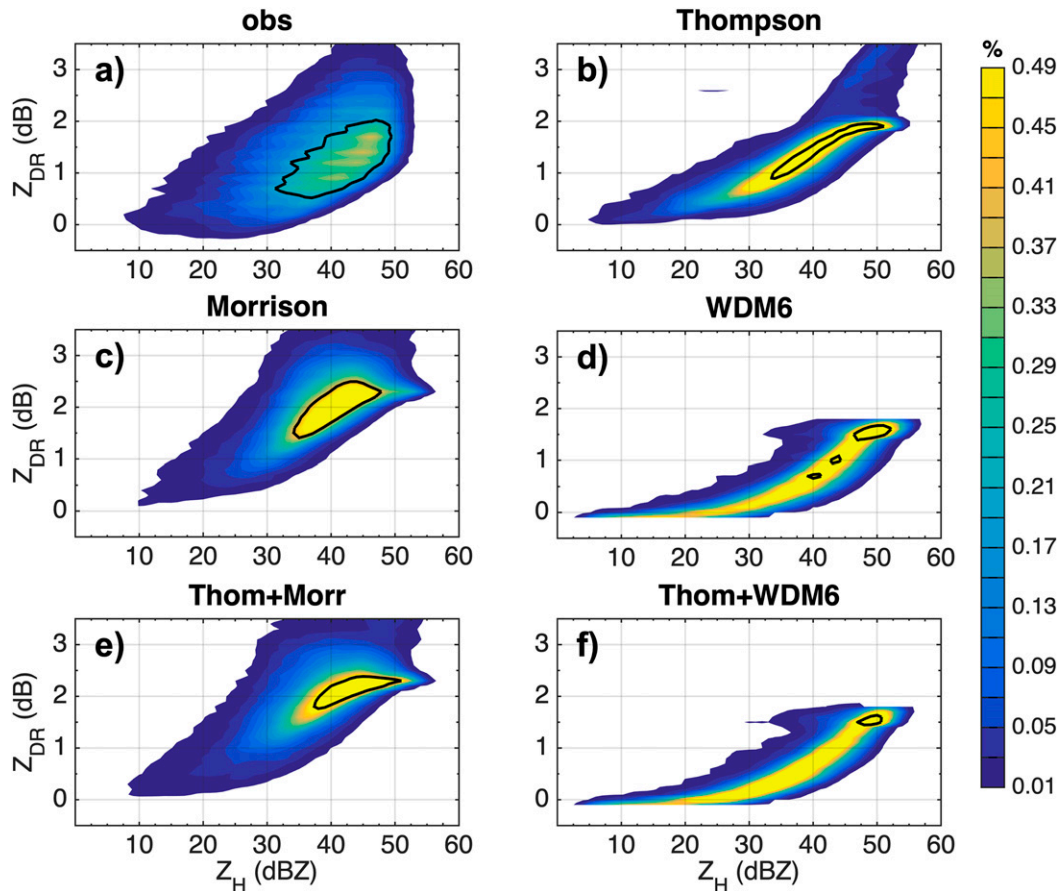


FIG. 5. As in Fig. 4, but for convective precipitation.

our study, the difference between the simulated and the observed Z_{DR} is not as large as in Brown et al. (2016). This difference can be attributed to the fact that the comparison in this study is only applicable for the outer rainband while the comparison in Brown et al. (2016) is for the full TC.

Although we focus on the model performance on the outer rainband in this study, one thing worth noting is that while the simulated reflectivity of the outer rainbands is similar to the observation, the simulated reflectivity of the inner core (Fig. 3a) is much larger than the observation. Also, the overestimation of the Z_{DR} in the inner core is more significant (not shown). The different performance of the same microphysical scheme in different region of the same TC suggests that different microphysical parameterizations are needed for the outer rainband and the inner core.

The Thom+Morr simulation (Fig. 4e) is similar to the Morrison (Fig. 4c), and the Thom+WDM6 simulation (Fig. 4f) resembles WDM6 (Fig. 4d). Although the rainband structure in these two experiments resemble that in Thompson by imposing the constraint of the large-scale environment (Figs. 3d–f), the resemblance of the PDF diagrams suggests that the microphysical properties of the precipitation respond quickly to and thus are controlled mainly by the microphysics schemes.

The precipitation in the rainband is further separated into convective and stratiform precipitation to have a more detailed

examination. Figure 5 shows the comparison of PDF for the convective precipitation in the outer rainband. In Fig. 5a, the peak frequency for observed convective precipitation is centered at 42 dBZ in Z_H and 1.3 dB in Z_{DR} . The modal distribution extends from 35 to 50 dBZ in Z_H and from 0.6 to 2.0 dB in Z_{DR} . For Thompson (Fig. 5b), the coordinate of the peak frequency along the Z_{DR} axis is just a bit higher than that of the observed PDF distribution, but the value of the peak frequency is much higher and more concentrated. Also, the occurrence frequency of points with larger Z_{DR} (>2.0 dB) is smaller than in the observations. These features indicate that raindrop sizes are overestimated in the Thompson scheme while the frequency of extremely large raindrops is deficient. Although the PDF diagram for Morrison (Fig. 5c) has as broad a distribution as observation, the peak frequency centers at a larger Z_{DR} (2.3 dB) than observation (1.3 dB), suggesting a significant overestimation of the raindrop sizes in this scheme. For WDM6 (Fig. 5d), the gamma shape distribution truncates the Z_{DR} value and the frequency for small Z_{DR} is higher than observation and other two schemes, which means the WDM6 scheme may produce too many small raindrops in convective precipitation compared to the observations.

Figure 6 compares the PDF for the stratiform precipitation in the outer rainband. In Fig. 6a, the Z_H and Z_{DR} for the peak

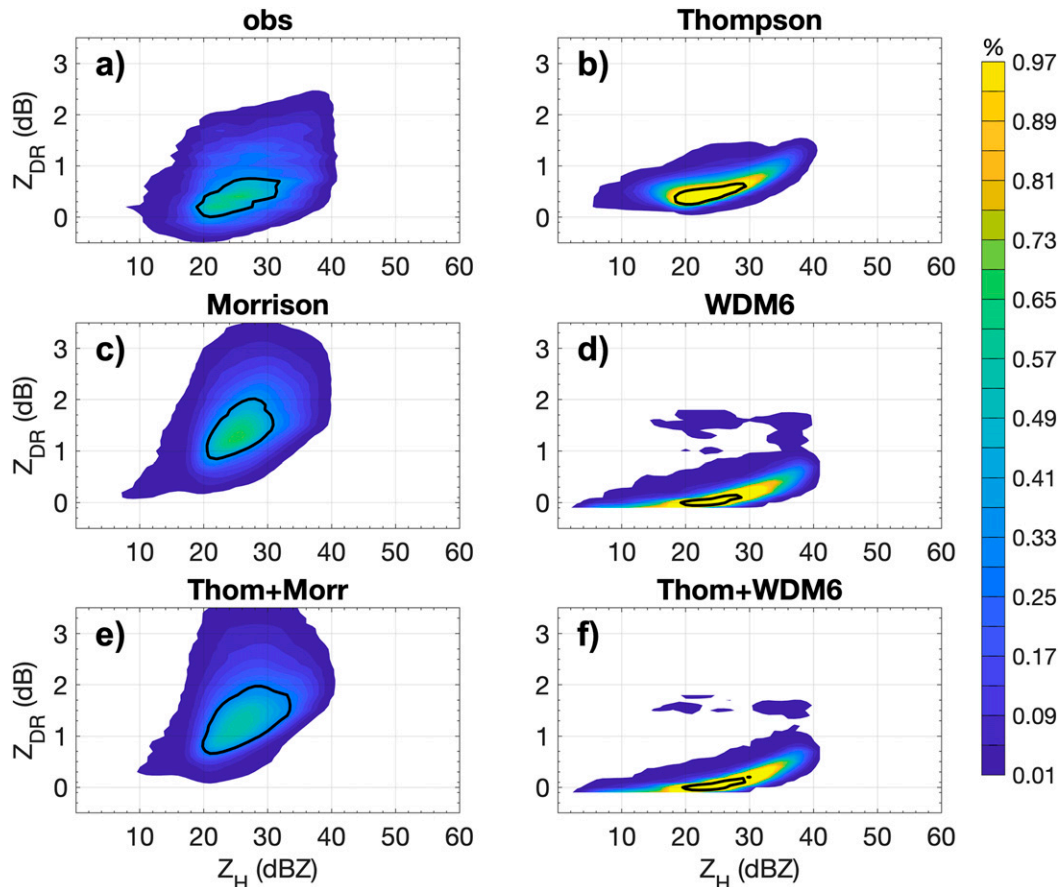


FIG. 6. As in Fig. 4, but for stratiform precipitation.

frequency are located between 20–30 dBZ and 0–0.8 dB, respectively. The Z_{DR} for the peak frequency almost remains constant with increasing Z_H , indicating a more uniform raindrop size distribution for the stratiform rainfall. The range of the modal distribution of the Thompson scheme (Fig. 6b) almost overlaps with the observed distribution. However, similar to the convective precipitation, the value of the frequency is much higher and more concentrated than that of the observation, suggesting the range of DSD types is also narrower in Thompson for stratiform precipitation. For Morrison (Fig. 6c), the peak frequency is located at a greater Z_{DR} (1.3 dB) than the observations, and the Z_{DR} for the peak frequency increases with Z_H , indicating larger raindrops for heavier rain, as expected (e.g., Kumjian 2013). For the WDM6 scheme (Fig. 6d) which produced less stratiform precipitation, the concentration of peak frequency around 20–30 dBZ in Z_H and 0.1 dB in Z_{DR} also indicates the simulated raindrop sizes are smaller than the observations in the stratiform precipitation.

The raindrops in Thompson and Morrison follow an inverse-exponential distribution, while in WDM6 that is a gamma distribution. The differences of the simulated PDF may be partly attributed to this assumption difference in these schemes, since the gamma distribution can substantially underestimate the

frequency of large raindrops. Thus, the PDF diagram of WDM6 seems to be truncated.

In Figs. 5e,f and 6e,f, the microphysical characteristics of the convective and stratiform precipitation for the two experiments constrained by Thompson schemes still resemble that of their matching single-scheme counterparts, emphasizing that the microphysics schemes have a dominant control on the microphysical properties of the precipitation.

c. Effect of raindrop size distribution on precipitation

Since the previous observational study (Wu et al. 2018) has demonstrated that the intense precipitation in the outer rainband is mainly produced by convective cells, we further investigate the impact of the simulated DSD on the surface precipitation intensity by comparing the convective precipitation in the outer rainband between the simulations and the observation. The LWC at the lowest level (0.5 km altitude), which is calculated based on the mixing ratio from the simulations, is used as a proxy for the rainfall intensity and compared with the estimation from observation. Since the result in Thom+Morr (Thom+WDM6) is similar to that in Morrison (WDM6) and is less affected by the differences in the large-scale environment when compared to the results in Thompson, the following analyses only present the results in Thompson, Thom+Morr, and Thom+WDM6.

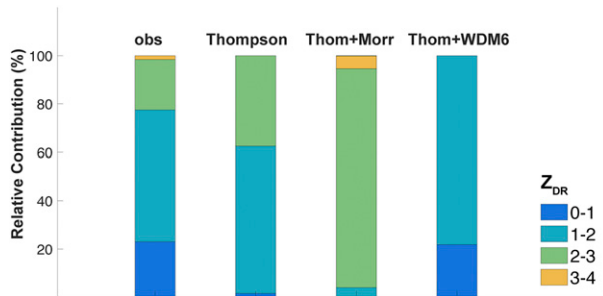


FIG. 7. Relative contribution to LWC at 0.5 km height from the raindrops with different sizes (scaled by Z_{DR}) for convective precipitation in the outer rainband.

The contribution to LWC at 0.5 km height in the convective precipitation of the outer rainband is decomposed by different sizes of raindrops (Fig. 7). The size of the raindrops is scaled by the value of Z_{DR} . For the observations, the largest contribution to LWC comes from data points with Z_{DR} values ranging from 1 to 3 dB. For the Thompson scheme, data points with Z_{DR} values ranging from 1 to 3 dB almost contribute 99% of the LWC. However, the percentage of the Z_{DR} values of 2–3 dB is much larger than in the observations while the contribution from $Z_{DR} < 1$ dB is much lower. Also, the contribution from $Z_{DR} > 3$ dB is marginal, consistent with the underestimation of the frequency for those large raindrops in the PDF diagram. For Thom+Morr, over 90% of the LWC is contributed by data points with Z_{DR} values ranging from 2 to 3 dB. Data with $Z_{DR} > 3$ dB also has a larger occurrence than in the observations. Therefore, in Thom+Morr, the rainfall with overestimated drop sizes (Fig. 6e) contributes more to the total rainfall. The LWC in the Thom+WDM6 is comprised of small raindrops with $Z_{DR} < 2$ dB. This decomposition of LWC by Z_{DR} (a proxy for raindrop sizes) for each simulation demonstrates that the raindrops with overestimated frequency by each scheme (Fig. 5) is the dominant component for the surface rainfall, meaning these biases have significant impacts on the simulated precipitation characteristics.

The evolution of the area-averaged LWC from each simulation is further calculated and normalized by the estimation from the observation (Fig. 8). The area average is performed for the convective precipitation in the outer rainband. It shows that the differences in the area-averaged LWC for the three experiments remain consistent during the 1 h analyses period. The Thom+WDM6 run has the smallest raindrops but the highest LWC, whereas the Thom+Morr simulation has the largest raindrops but the smallest LWC. The simulated mean rain number concentration ($N_{r,35}$) at the grid points with 35 dBZ was 1074 kg^{-1} for Thom+WDM6, 1034 kg^{-1} for Thompson, and 74 kg^{-1} for Thom+Morr, which shows that the simulation with larger raindrops has lower water content because of the lower number concentration. Thus, the erroneous DSDs produced by the microphysics schemes are correlated with the simulated surface precipitation intensity.

d. Comparison of vertical profiles of water content

The microphysical properties and intensity of surface precipitation are determined by the microphysical processes ongoing

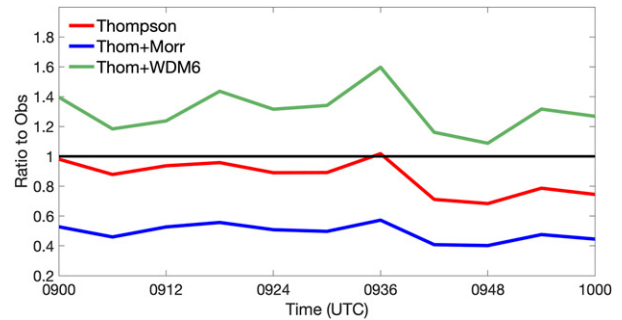


FIG. 8. The evolution of the normalized LWC (normalized by the LWC estimation from the observation) at 0.5 km height for Thompson (red), Thom+Morr (blue), and Thom+WDM6 (green). The LWC is averaged in the region of convective precipitation.

aloft. To find out the potential sources for the model deviation from the observed precipitation, the vertical structures from the simulations and observations are compared.

Figure 9 shows the median profiles of polarimetric variables for the observed convective precipitation. The primary particle growth processes can be inferred by these profiles (e.g., Wang et al. 2016; Wu et al. 2018). Above 12 km altitude, the prevalent particles are the pristine ice crystals formed by deposition. In the 12–8 km layer, the increasing Z_H and decreasing Z_{DR} with decreasing height indicates the pristine ice crystals transforming into snow aggregates (e.g., Schrom et al. 2015; Kumjian and Lombardo 2017). Between 8 km and the 0°C level, the increasing median Z_{DR} and K_{DP} toward the 0°C level likely reflects Z_{DR} and K_{DP} columns, which indicate the existence of supercooled liquid drops (Kumjian et al. 2014; Van Lier-Walqui et al. 2016); the increase of Z_H reflects the possible occurrence of riming.

Because the treatments of ice phase particles are still very simplified in the polarimetric radar simulator, and because the microphysics schemes do not explicitly predict necessary information for calculating the polarimetric radar variables in ice (e.g., highly uncertain particle shapes, orientations), the simulated polarimetric variables above the 0°C level are not suitable for quantitative evaluation. Alternatively, the IWC and LWCs in each simulation are calculated to compare with the estimation from the observational retrieval. Figure 10a shows the median profile of the IWC for the convective precipitation in the outer rainband. Since the retrieval algorithm may be inaccurate in the mixed-phase precipitation where riming is significant (see red shading in Figs. 9 and 10a), an upper threshold of 40 dBZ is used for Z_H above 5.5 km altitude to avoid including graupel or small hail produced by riming. Correspondingly, graupel can be explicitly excluded from IWC in simulations by only including snow and cloud ice determined by the microphysics schemes in the calculation of IWC for each simulation. Although the estimated IWC may have significant biases/uncertainties, the different vertical gradient of the estimated and simulated water contents (rather than absolute values) shed some light on the differences of the ice-phase microphysical processes between simulations. In the layer

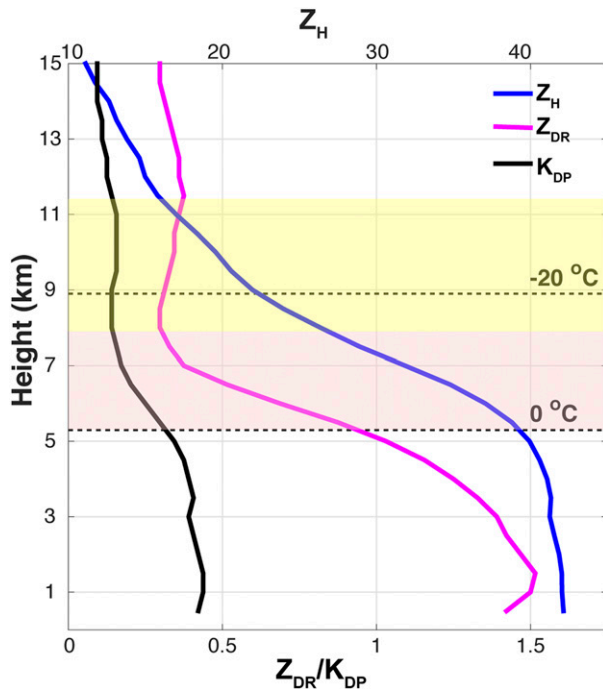


FIG. 9. The vertical profiles of median Z_H (dBZ), Z_{DR} (dB), and K_{DP} ($^{\circ} \text{km}^{-1}$) of the observed convective precipitation in the outer rainband. The two black dashed lines represent the levels of -20° and 0°C , respectively. The yellow and red shadings denote the “aggregation zone” and “riming zone,” respectively.

above the -20°C level up to 15 km altitude, the IWC retrieved from observation is larger than all the three simulations, suggesting the simulations fail to adequately represent the ice-phase microphysical processes in the outer rainband of a real TC, and/or the retrieval algorithm has a positive bias. This distinct difference in the layer above 12 km altitude, where deposition is dominant, suggests the concentration or growth of very small ice crystals may be significantly underestimated in the simulations. This is not surprising, given the simplified treatment of vapor growth in such schemes (e.g., see discussions in Harrington et al. 2013). Besides, another important ice multiplication mechanism known as secondary ice production (SIP) is also not well represented in the bulk microphysical schemes (Field et al. 2017). Below 12 km altitude, the IWC increases with decreasing height in the aggregation zone (8–12 km). Although the IWC retrieved from the observation may be underestimated due to the upper threshold, the simulated IWC in Thom+Morr and Thom+WDM6 is still smaller than the estimation. However, the gradient is sharper in all the three simulations, especially in the Thompson scheme. The decomposition of the total IWC shows that this increase is caused by the increase of snow and the growth rate of snow from deposition is largest in this layer (not shown), which indicates that there is more water vapor transferred into snow by the Thompson microphysics scheme than in the observations. Since the IWC for hail and graupel is excluded in this study, the variation of IWC is not discussed in the riming zone (red shading). However, some studies found

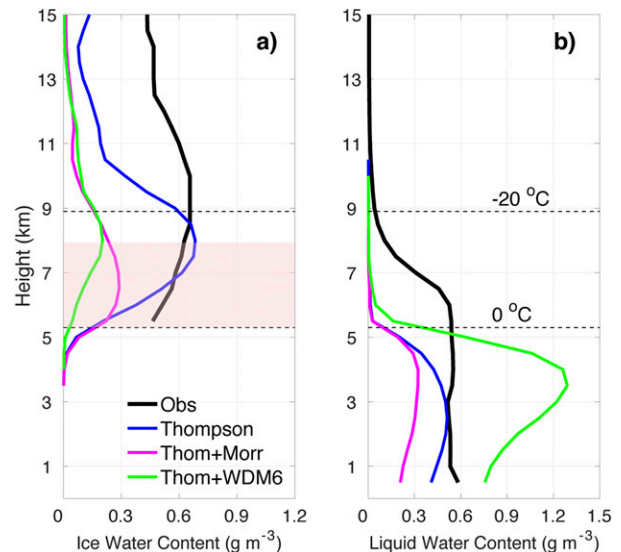


FIG. 10. The median profiles of (a) ice water content and (b) liquid water content for the convective precipitation in the outer rainband. The thick black line represents the water content estimations from the observation. The upper and lower horizontal black dashed lines mark the levels of -20° and 0°C in the outer rainband environment, respectively. The red shading denotes the riming region where retrieved IWC from the observation is of great uncertainties.

that the microphysical schemes tend to overproduce graupel in TCs (McFarquhar et al. 2006, 2012; Brown et al. 2016), which may be an important error source for model simulations. Further evaluation for this issue is necessary in the future.

The warm-rain processes below 0°C level inferred from the median profiles of LWC in the convective precipitation are also compared and shown in Fig. 10b. Since the algorithm is only valid for pure rain, the estimated LWC from observation may be inaccurate above and near the 0°C level. Notably, the estimated LWC from the observations almost does not vary below the 0°C level. The slight change of LWC indicates that the warm-rain processes are not as important as the ice-phase processes in the outer rainband (Wu et al. 2018). A similar feature is also found in Thompson and Thom+Morr, in which the LWC profiles change slightly below 4 and 4.5 km altitude, respectively. However, the LWC profiles for Thom+WDM6 are quite different: LWC increases substantially with decreasing height just below 0°C , and the LWC maximum is even larger than the IWC maximum above the 0°C level. Below the maximum level (~ 3.5 km altitude), the LWC decreases sharply toward the ground. Such a dramatic change suggests that the warm-rain processes (including accretion of cloud water and evaporation) are much more active and efficient in the WDM6 scheme.

The comparison between the vertical profiles of the estimated and simulated IWC shows that the ice-phase processes are underestimated in all schemes. This insufficient ice production in these simulations may contribute to the underestimated surface precipitation. To illustrate this deficiency more clearly, a more detailed comparison is made between the

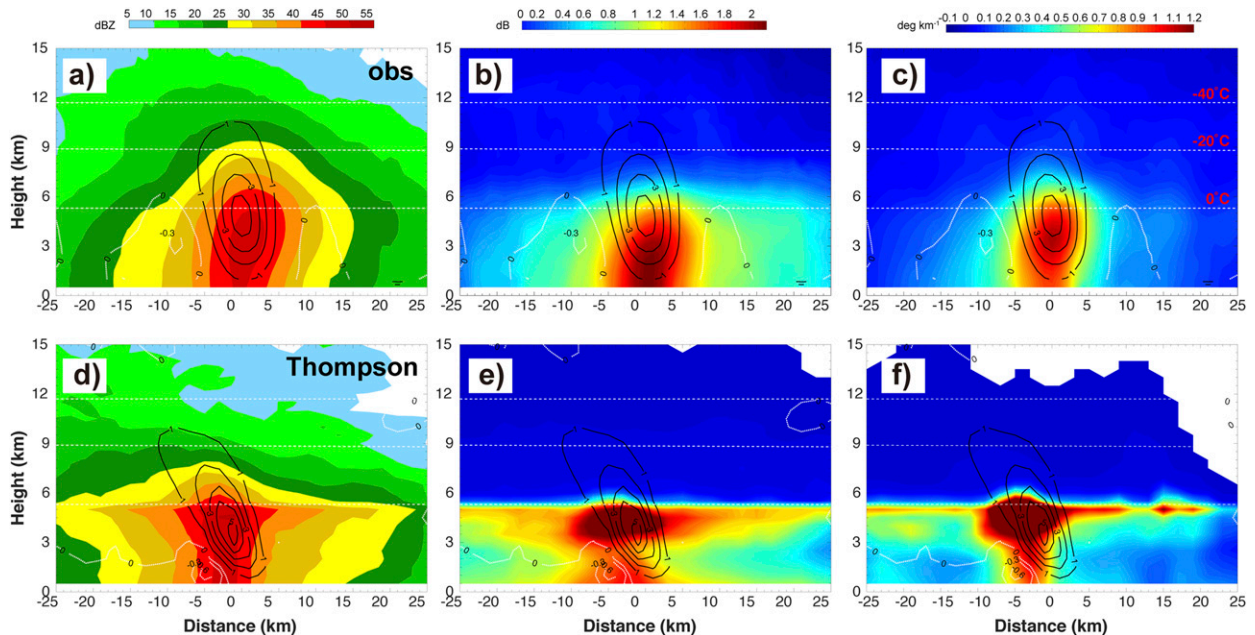


FIG. 11. Composite-mean vertical cross sections of (left) Z_H (in dBZ), (center) Z_{DR} (in dB), and (right) K_{DP} (in $^{\circ}\text{km}^{-1}$) of the mature convective cells along the propagation direction of the (a)–(c) observed and (d)–(f) simulated outer rainband using Thompson scheme. The negative values along the x axis correspond to the rearward side of the composite convective cell relative to the propagation direction. The black contours represent vertical velocity at 1 m s^{-1} intervals for updraft and the white dashed contours at 0.3 m s^{-1} intervals for downdraft. The horizontal white dashed lines indicate altitudes corresponding to -40° , -20° , and 0°C from top to bottom, respectively.

output from the Thompson test and the observation. The top panels in Fig. 11 are the composite-mean vertical cross section of Z_H , Z_{DR} , and K_{DP} of the mature convective cells in the observed outer rainband while the bottom panels are that in the simulated outer rainband by the Thompson scheme. The black line across the outer rainband in Fig. 3a marks the location of one example of the cross section. The black contours in Fig. 11 represent the composite vertical velocity for the updrafts. Although the vertical velocities in the updraft region tended to be overestimated above 6 km altitude (Oue et al. 2019), it can be seen that the simulated updraft in the observed and simulated convective cells are quite similar in terms of the rearward tilt and the updraft intensity. However, the magnitude of the simulated Z_H is smaller than the observation above the 0°C level, indicating that there are fewer or smaller ice particles in the simulation. Z_{DR} and K_{DP} are shown for completeness, but recall that the forward operator has far too great uncertainty when ice particles are involved (e.g., the odd vertical structure of the simulated Z_{DR} and K_{DP} just below the freezing level at $|\text{Distance}| > 5\text{ km}$) and thereby a quantitative comparison is not allowed. Figure 12 shows the composite-mean vertical cross sections of the estimated IWC, as in Fig. 11. In the updraft, the IWC with value greater 0.4 g m^{-3} extends to 12 km altitude, implying that the ice-phase processes are active in the observed convective cells. Figure 13 shows the composite-mean vertical cross sections of IWC from the Thompson test. The simulated total IWC (Fig. 13a) also has a high concentration in the convective updraft while the vertical extension of $\text{IWC} > 0.4\text{ g m}^{-3}$ lower than that of the estimates

from the observation. The total IWC is decomposed into ice, snow, and graupel/hail (Figs. 13b–d), respectively. The distribution of these hydrometeors is organized systematically relative to the convective updraft. The graupel/hail is mostly concentrated within the updraft and the snow prevails around the -15°C level, which is quite similar to the findings based on polarimetric radar

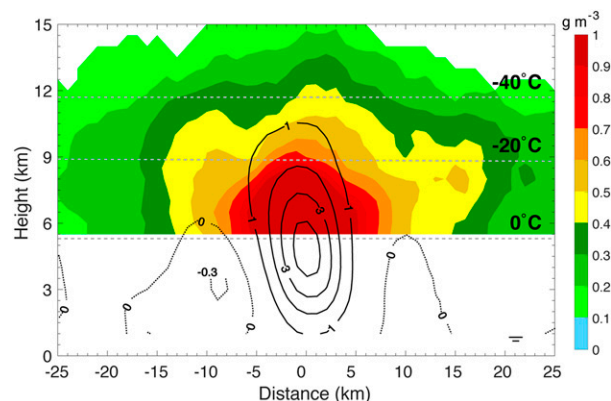


FIG. 12. Composite-mean vertical cross section of estimated IWC of the mature convective cells along the motion direction of the observed outer rainband. The negative value along the x axis corresponds to the rear side of the composite convective cell. The black contours represent vertical velocity at 1 m s^{-1} intervals for updraft and the dashed lines represent vertical velocity at 0.3 m s^{-1} intervals for downdraft. Horizontal dashed lines indicate altitudes corresponding to -40° , -20° , and 0°C from top to bottom, respectively.

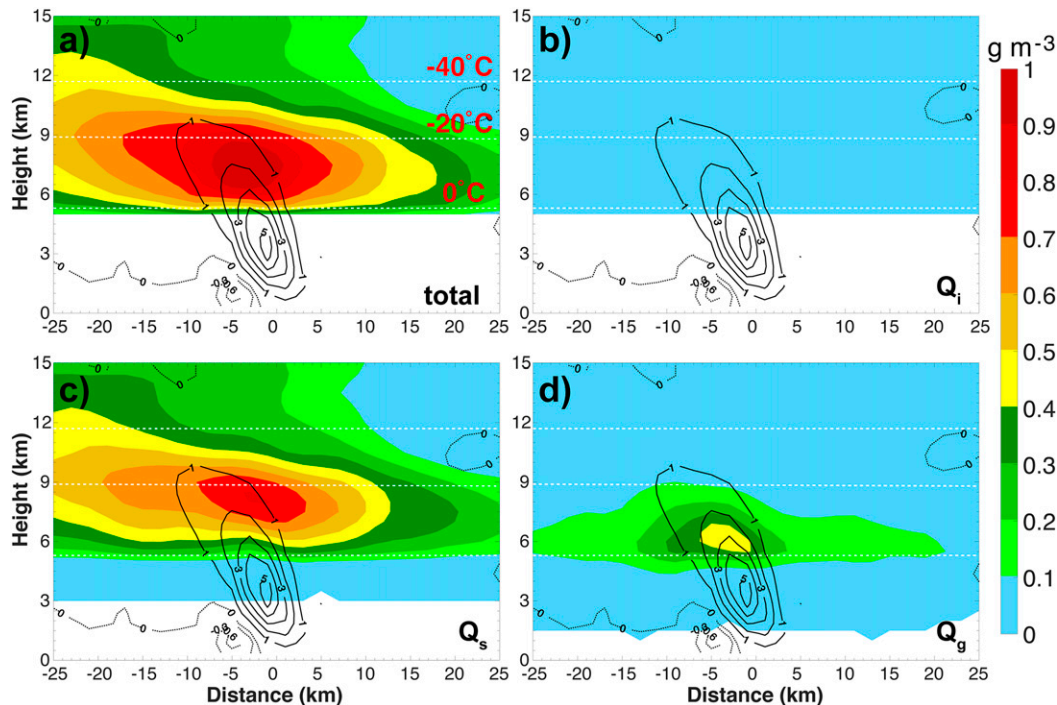


FIG. 13. Composite-mean vertical cross sections of IWC for (a) total, (b) ice, (c) snow, and (d) graupel and hail of the mature convective cells along the propagation direction of the simulated outer rainband in Thompson. The solid black contours at 1 m s^{-1} intervals represent updrafts. The dashed contours at 0.3 m s^{-1} intervals denote downdrafts. Horizontal white dashed lines indicate altitudes corresponding to -40° , -20° , and 0°C from top to bottom, respectively.

observations by [Wu et al. \(2018\)](#). However, the IWC in the ice region (above 12 km) is much smaller ($<10^{-3} \text{ g m}^{-3}$). The detailed comparison between the observation and the Thompson simulation supports the argument that the concentration of very small ice crystals is underestimated in the simulations.

4. Summary and conclusions

This study evaluates three double-moment microphysics schemes, i.e., Thompson, Morrison, and WDM6, regarding the microphysical characteristics of the precipitation in the outer rainband of Typhoon Nida (2016). A series of numerical simulations are performed and all of them generally capture the tracks, intensity changes, and the outer rainband structure. However, the microphysical characteristics of raindrops and the surface precipitation intensity differ significantly from the polarimetric radar observations.

Results indicate that discrepancies introduced by the long-term integration do not impact the drop size distributions (DSDs), and the microphysical characteristics of the precipitation are mainly determined by microphysics schemes. None of the schemes successfully reproduce the observed polarimetric radar signatures. By comparing the joint probability density function of Z_H and Z_{DR} from simulation and GZRD observation, the median raindrop size in Morrison is found to be much larger than that in the observation. The median raindrop size in Thompson is slightly larger while the occurrence frequency for the extreme large raindrops is smaller than

observations. In comparison, WDM6 produces much smaller raindrops. This may be partly attributed to the assumption of the raindrop size distributions in these schemes. The microphysical schemes fail to reproduce the accurate DSD, which has a direct impact on the surface rain rate. One new finding in this study is the area-averaged liquid water content (LWC) of the convective precipitation in the outer rainband increases as the mean raindrop size decreases. For the overestimated raindrop sizes in Morrison and Thompson, the area-averaged LWC is smaller than observation. In contrast, the LWC is largest and the raindrop sizes are smallest in WDM6. These discrepancies are closely related to the rigid assumptions about fixed DSD shapes (i.e., exponential or gamma function) in these microphysics schemes, whereas natural variability is likely much greater than allowed by such assumptions (see the discussion in [Kumjian et al. 2019](#)).

The comparison of the ice water content (IWC) and LWC indicates that the misrepresented DSD is substantially affected by the differences of the microphysical processes above the 0°C level. The simulated IWC (graupel/hail not included) above the 0°C level is smaller than estimated from the observations, especially in the layer above 12 km where growth by vapor deposition is dominant. This fact suggests that the concentration of pristine ice particles is underestimated by the microphysics schemes. However, the relatively large increase in IWC with decreasing height in the 8–12 km layer in Thompson scheme compared to the other two schemes indicates that more water vapor is converted into snow in this layer. Compared with the estimates from observation, these differences in IWC and ice-

phase microphysical processes likely contribute to an underestimated surface rain rate characterized by a lower concentration of larger raindrops in the Thompson and Morrison schemes. The more active warm-rain processes (e.g., accretion and evaporation) in WDM6 seemingly offset this effect and produce even smaller raindrops than inferred from the observations.

Although the IWC retrieval method adopted in this study is state-of-the-art, uncertainties still exist for the IWC estimation in the riming region, where a quantitative comparison between observations and simulations in this layer is excluded in this study. Given microphysical schemes tend to overproduce graupel in tropical cyclones (McFarquhar et al. 2006, 2012; Brown et al. 2016), developing better retrieval methods and collecting more in situ observations in the riming region are highly desired in the future. Additionally, nonlocal processes, such as upper-level transportation, may partly affect the estimation of IWC in the midupper troposphere. Discussions of this uncertainty is left to future work. Of note, while the resolution of radar data degrades at a longer distance, composite vertical profiles of polarimetric variables for the convective cells at different radii are very similar (not shown), suggesting that results in this study are not sensitive to the data resolution. Finally, we recognize that the findings are based on one case study, whether they can be generally applied to other cases is an important topic to further explore. To improve the forecast of TC precipitation, we recommend the TC community to perform a systematic examination of the parameterizations of ice-phase processes in the microphysics schemes.

Acknowledgments. This work was primarily supported by the National Key Research and Development Program of China under Grants 2018YFC1506404, Key Program for International S&T Cooperation Projects of China (Grant 2017YFE0107700 and 2020YFE0201900), the National Natural Science Foundation of China (Grants 41705036, 42025501, 41605033, 41875053, 41775064, 41775065, and 41875080), the Open Research Program of the State Key Laboratory of Severe Weather, the 5th “333 High-level Personnel Training Project” of Jiangsu Province (BRA2019037), the Fundamental Research Funds for the Central Universities, Typhoon Scientific and Technological Innovation Group of Shanghai Meteorological Service, the Research Grants Council of the Hong Kong Special Administrative Region of China Grant City (U11301417), and Scientific Research Program of Shanghai Science and Technology Commission (19dz1200101). The authors acknowledge the Texas Advanced Computing Center (TACC) at the University of Texas at Austin for providing computing and storage resources that have contributed to the research results reported within this paper. We also want to acknowledge Dr. Frank D. Marks for his valuable suggestions to improve this manuscript.

REFERENCES

- Black, R. A., and J. Hallett, 1986: Observations of the distribution of ice in hurricanes. *J. Atmos. Sci.*, **43**, 802–822, [https://doi.org/10.1175/1520-0469\(1986\)043<0802:OOTDOI>2.0.CO;2](https://doi.org/10.1175/1520-0469(1986)043<0802:OOTDOI>2.0.CO;2).
- Brown, B. R., M. M. Bell, and A. J. Frambach, 2016: Validation of simulated hurricane drop size distributions using polarimetric radar. *Geophys. Res. Lett.*, **43**, 910–917, <https://doi.org/10.1002/2015GL067278>.
- Chen, X., Y. Wang, K. Zhao, and D. Wu, 2017: A numerical study on rapid intensification of Typhoon Vicente (2012) in the South China Sea. Part I: Verification of simulation, storm-scale evolution, and environmental contribution. *Mon. Wea. Rev.*, **145**, 877–898, <https://doi.org/10.1175/MWR-D-16-0147.1>.
- DeMaria, M., M. Mainelli, L. K. Shay, J. A. Knaff, and J. Kaplan, 2005: Further improvements to the Statistical Hurricane Intensity Prediction Scheme (SHIPS). *Wea. Forecasting*, **20**, 531–543, <https://doi.org/10.1175/WAF862.1>.
- Didlake, A. C., Jr., and M. R. Kumjian, 2017: Examining polarimetric radar observations of bulk microphysical structures and their relation to vortex kinematics in Hurricane Arthur (2014). *Mon. Wea. Rev.*, **145**, 4521–4541, <https://doi.org/10.1175/MWR-D-17-0035.1>.
- , and —, 2018: Examining storm asymmetries in Hurricane Irma (2017) using polarimetric radar observations. *Geophys. Res. Lett.*, **45**, 13 513–13 522, <https://doi.org/10.1029/2018GL080739>.
- Doviak, R. J., and D. S. Zrnić, 1993: *Doppler Radar & Weather Observations*. 2nd ed. Academic Press, 562 pp.
- Duan, Y., and J. Liu, 2010: TC precipitation (QPE/QPF) and related inland flood modeling. *Seventh Int. Workshop on Tropical Cyclones (IWTC-VII)*, La Réunion, France, World Meteorological Organization, 79 pp., https://library.wmo.int/doc_num.php?explnum_id=9780.
- Dudhia, J., 1989: Numerical study of convection observed during the Winter Monsoon Experiment using a mesoscale two-dimensional model. *J. Atmos. Sci.*, **46**, 3077–3107, [https://doi.org/10.1175/1520-0469\(1989\)046<3077:NSOCOD>2.0.CO;2](https://doi.org/10.1175/1520-0469(1989)046<3077:NSOCOD>2.0.CO;2).
- Feng, Y.-C., and M. M. Bell, 2019: Microphysical characteristics of an asymmetric eyewall in major Hurricane Harvey (2017). *Geophys. Res. Lett.*, **46**, 461–471, <https://doi.org/10.1029/2018GL080770>.
- Field, P. R., and Coauthors, 2017: Secondary ice production: Current state of the science and recommendations for the future. *Ice Formation and Evolution in Clouds and Precipitation: Measurement and Modeling Challenges*, Meteor. Monogr., No. 58, Amer. Meteor. Soc., <https://doi.org/10.1175/AMSMONOGRAPHIS-D-16-0014.1>.
- Franklin, J. L., C. J. McAdie, and M. B. Lawrence, 2003: Trends in track forecasting for tropical cyclones threatening the United States, 1970–2001. *Bull. Amer. Meteor. Soc.*, **84**, 1197–1204, <https://doi.org/10.1175/BAMS-84-9-1197>.
- Harrington, J. Y., K. Sulia, and H. Morrison, 2013: A method for adaptive habit prediction in bulk microphysical models. Part I: Theoretical development. *J. Atmos. Sci.*, **70**, 349–364, <https://doi.org/10.1175/JAS-D-12-040.1>.
- Hong, S.-Y., Y. Noh, and J. Dudhia, 2006: A new vertical diffusion package with an explicit treatment of entrainment processes. *Mon. Wea. Rev.*, **134**, 2318–2341, <https://doi.org/10.1175/MWR3199.1>.
- Houze, R. A., 2010: Clouds in tropical cyclones. *Mon. Wea. Rev.*, **138**, 293–344, <https://doi.org/10.1175/2009MWR2989.1>.
- Huang, H., G. Zhang, K. Zhao, and S. E. Giangrande, 2017: A hybrid method to estimate specific differential phase and rainfall with linear programming and physics constraints. *IEEE Trans. Geosci. Remote Sens.*, **55**, 96–111, <https://doi.org/10.1109/TGRS.2016.2596295>.
- Jung, Y., M. Xue, and G. Zhang, 2010: Simulations of polarimetric radar signatures of a supercell storm using a two-moment bulk microphysics scheme. *J. Appl. Meteor. Climatol.*, **49**, 146–163, <https://doi.org/10.1175/2009JAMC2178.1>.
- Kain, J. S., and J. M. Fritsch, 1993: Convective parameterization for mesoscale models: The Kain–Fritsch scheme. *The Representation*

- of *Cumulus Convection in Numerical Models*, Meteor. Monogr., No. 24, Amer. Meteor. Soc., 165–170.
- Kalina, E. A., and Coauthors, 2017: The ice water paths of small and large ice species in Hurricanes Arthur (2014) and Irene (2011). *J. Appl. Meteor. Climatol.*, **56**, 1383–1404, <https://doi.org/10.1175/JAMC-D-16-0300.1>.
- Kumjian, M. R., 2013: Principles and applications of dual-polarization weather radar. Part I: Description of the polarimetric radar variables. *J. Oper. Meteor.*, **1**, 226–242, <https://doi.org/10.15191/nwajom.2013.0119>.
- , and A. V. Ryzhkov, 2010: The impact of evaporation on polarimetric characteristics of rain: Theoretical model and practical implications. *J. Appl. Meteor. Climatol.*, **49**, 1247–1267, <https://doi.org/10.1175/2010JAMC2243.1>.
- , and O. P. Prat, 2014: The impact of raindrop collisional processes on the polarimetric radar variables. *J. Atmos. Sci.*, **71**, 3052–3067, <https://doi.org/10.1175/JAS-D-13-0357.1>.
- , and K. A. Lombardo, 2017: Insights into the evolving microphysical and kinematic structure of Northeastern U.S. winter storms from dual-polarization Doppler radar. *Mon. Wea. Rev.*, **145**, 1033–1061, <https://doi.org/10.1175/MWR-D-15-0451.1>.
- , A. P. Khain, N. Benmoshe, E. Ilotoviz, A. V. Ryzhkov, and V. T. J. Phillips, 2014: The anatomy and physics of Z_{DR} columns: Investigating a polarimetric radar signature with a spectral bin microphysical model. *J. Appl. Meteor. Climatol.*, **53**, 1820–1843, <https://doi.org/10.1175/JAMC-D-13-0354.1>.
- , C. P. Martinkus, O. P. Prat, S. Collis, M. van Lier-Walqui, and H. C. Morrison, 2019: A moment-based polarimetric radar forward operator for rain microphysics. *J. Appl. Meteor. Climatol.*, **58**, 113–130, <https://doi.org/10.1175/JAMC-D-18-0121.1>.
- Lim, K.-S. S., and S.-Y. Hong, 2010: Development of an effective double-moment cloud microphysics scheme with prognostic cloud condensation nuclei (CCN) for weather and climate models. *Mon. Wea. Rev.*, **138**, 1587–1612, <https://doi.org/10.1175/2009MWR2968.1>.
- May, P. T., J. D. Kepert, and T. D. Keenan, 2008: Polarimetric radar observations of the persistently asymmetric structure of Tropical Cyclone Ingrid. *Mon. Wea. Rev.*, **136**, 616–630, <https://doi.org/10.1175/2007MWR2077.1>.
- McFarquhar, G. M., and R. A. Black, 2004: Observations of particle size and phase in tropical cyclones: Implications for mesoscale modeling of microphysical processes. *J. Atmos. Sci.*, **61**, 422–439, [https://doi.org/10.1175/1520-0469\(2004\)061<0422:OOPSAP>2.0.CO;2](https://doi.org/10.1175/1520-0469(2004)061<0422:OOPSAP>2.0.CO;2).
- , H. Zhang, G. Heymsfield, J. B. Halverson, R. Hood, J. Dudhia, and F. Marks Jr., 2006: Factors affecting the evolution of Hurricane Erin (2001) and the distributions of hydrometeors: Role of microphysical processes. *J. Atmos. Sci.*, **63**, 127–150, <https://doi.org/10.1175/JAS3590.1>.
- , B. F. Jewett, M. S. Gilmore, S. W. Nesbitt, and T.-L. Hsieh, 2012: Vertical velocity and microphysical distributions related to rapid intensification in a simulation of Hurricane Dennis (2005). *J. Atmos. Sci.*, **69**, 3515–3534, <https://doi.org/10.1175/JAS-D-12-016.1>.
- Mlawer, E. J., S. J. Taubman, P. D. Brown, M. J. Iacono, and S. A. Clough, 1997: Radiative transfer for inhomogeneous atmospheres: RRTM, a validated correlated-k model for the longwave. *J. Geophys. Res.*, **102**, 16663–16682, <http://doi.org/10.1029/97JD00237>.
- Mohr, C. G., L. Jay Miller, R. L. Vaughan, and H. W. Frank, 1986: The merger of mesoscale datasets into a common Cartesian format for efficient and systematic analyses. *J. Atmos. Oceanic Technol.*, **3**, 143–161, [https://doi.org/10.1175/1520-0426\(1986\)003<0143:TMOMDI>2.0.CO;2](https://doi.org/10.1175/1520-0426(1986)003<0143:TMOMDI>2.0.CO;2).
- Morrison, H., G. Thompson, and V. Tatarskii, 2009: Impact of cloud microphysics on the development of trailing stratiform precipitation in a simulated squall line: Comparison of one- and two-moment schemes. *Mon. Wea. Rev.*, **137**, 991–1007, <https://doi.org/10.1175/2008MWR2556.1>.
- Oue, M., P. Kollias, A. Shapiro, A. Tatarevic, and T. Matsui, 2019: Investigation of observational error sources in multi-Doppler-radar three-dimensional variational vertical air motion retrievals. *Atmos. Meas. Tech.*, **12**, 1999–2018, <https://doi.org/10.5194/amt-12-1999-2019>.
- Oye, R., C. Mueller, and S. Smith, 1995: Software for radar translation, visualization, editing, and interpolation. Preprints, *27th Conf. on Radar Meteorology*, Vail, CO, Amer. Meteor. Soc., 359–361.
- Ray, P. S., K. K. Wagner, K. W. Johnson, J. J. Stephens, W. C. Bumgarner, and E. A. Mueller, 1978: Triple-Doppler observations of a convective storm. *J. Appl. Meteor.*, **17**, 1201–1212, [https://doi.org/10.1175/1520-0450\(1978\)017<1201:TDOOC>2.0.CO;2](https://doi.org/10.1175/1520-0450(1978)017<1201:TDOOC>2.0.CO;2).
- Ryzhkov, A., P. Bukovic, A. Murphy, P. Zhang, and G. McFarquhar, 2018: Ice microphysical retrievals using polarimetric radar data. *10th European Conf. on Radar in Meteorology and Hydrology*, Netherlands, KNMI, 40, https://projects.knmi.nl/erad2018/ERAD2018_extended_abstract_040.pdf.
- Ryzhkov, A. V., J. Snyder, J. T. Carlin, A. Khain, and M. Pinsky, 2020: What polarimetric weather radars offer to cloud models: Forward radar operators and microphysical/thermodynamic retrievals. *Atmosphere*, **11**, 362, <https://doi.org/10.3390/atmos11040362>.
- Schrom, R. S., M. R. Kumjian, and Y. Lu, 2015: Polarimetric radar signatures of dendritic growth zones within Colorado winter storms. *J. Appl. Meteor. Climatol.*, **54**, 2365–2388, <https://doi.org/10.1175/JAMC-D-15-0004.1>.
- Seliga, T. A., and V. N. Bringi, 1976: Potential use of radar differential reflectivity measurements at orthogonal polarizations for measuring precipitation. *J. Appl. Meteor.*, **15**, 69–76, [https://doi.org/10.1175/1520-0450\(1976\)015<0069:PUORDR>2.0.CO;2](https://doi.org/10.1175/1520-0450(1976)015<0069:PUORDR>2.0.CO;2).
- Skamarock, W. C., and Coauthors, 2008: A description of the Advanced Research WRF version 3. NCAR Tech. Note NCAR/TN-475+STR, 113 pp., <https://doi.org/10.5065/D68S4MVH>.
- Steiner, M., R. A. Houze Jr., and S. E. Yuter, 1995: Climatological characterization of three-dimensional storm structure from operational radar and rain gauge data. *J. Appl. Meteor.*, **34**, 1978–2007, [https://doi.org/10.1175/1520-0450\(1995\)034<1978:CCOTDS>2.0.CO;2](https://doi.org/10.1175/1520-0450(1995)034<1978:CCOTDS>2.0.CO;2).
- Thompson, G., P. R. Field, R. M. Rasmussen, and W. D. Hall, 2008: Explicit forecasts of winter precipitation using an improved bulk microphysics scheme. Part II: Implementation of a new snow parameterization. *Mon. Wea. Rev.*, **136**, 5095–5115, <https://doi.org/10.1175/2008MWR2387.1>.
- Van Lier-Walqui, M., and Coauthors, 2016: On polarimetric radar signatures of deep convection for model evaluation: Columns of specific differential phase observed during MC3E. *Mon. Wea. Rev.*, **144**, 737–758, <https://doi.org/10.1175/MWR-D-15-0100.1>.
- Wang, M., K. Zhao, M. Xue, G. Zhang, S. Liu, L. Wen, and G. Chen, 2016: Precipitation microphysics characteristics of a Typhoon Matmo (2014) rainband after landfall over Eastern China based on polarimetric radar observations. *J. Geophys. Res. Atmos.*, **121**, 12 415–12 433, <https://doi.org/10.1002/2016JD025307>.
- Wu, D., and Coauthors, 2018: Kinematics and microphysics of convection in the outer rainband of Typhoon Nida (2016) revealed by polarimetric radar. *Mon. Wea. Rev.*, **146**, 2147–2159, <https://doi.org/10.1175/MWR-D-17-0320.1>.
- Zhang, G., 2016: *Weather Radar Polarimetry*. CRC Press, 304 pp.